Biointerface Research in Applied Chemistry
Platinum Open Access Journal (ISSN: 2069-5837)

Article
Volume 12, Issue 1, 2022, 929 - 939
https://doi.org/10.33263/BRIAC121.929939

Crystal Chemistry, Magnetic and Dielectric Properties of Nickel Doped Strontium Ferrites

Maramu Nyathani [1], Gaddameedi Sriramulu [1], Tadiboyina Anil Babu [3], Narasipuram VenkataKrishna Prasad [3], Dachepalli Ravinder [2,*], Sadhana Katlakunta [1,*]

[1] Department of Physics, University College of Science, Saifabad, Osmania University, Hyderabad-500004, Telangana, India
[2] Department of Physics, Osmania University, Hyderabad-500007, Telangana, India
[3] Department of Physics, GITAM Deemed to be University, Bangalore, Karnataka-562163, India
* Correspondence: sadhanaphysics@gmail.com (S.K.); ravindergupta28@rediffmail.com (D.R.);
Scopus Author ID 57190787752

Received: 1.03.2021; Revised: 10.04.2021; Accepted: 15.04.2021; Published: 26.04.2021

Abstract: The $SrNi_xFe_{12-2x}O_{19}$ (where x = 0.0–0.8) hexaferrites powders were synthesized using Co-precipitation method and the pellets were prepared at 1100 °C/4 h in muffle furnace. XRD, FTIR, SEM and EDS analysis were used to analyze the samples structural parameters. The changes in the lattice parameters *'a'*&*'c'* are due to the differences in ionic radii. The average grain size (<D>) was estimated from SEM images and found to be in between 1.713 µm (x = 0) - 0.549 µm (x = 1.0). Observations indicated a decrease in saturation magnetization decreased from 68 emu/g (x = 0.0) to 50 emu/g (x = 0.6) and for x > 0.6, M_S increases to 64 emu/g (x = 0.8). The coercivity exhibit anisotropic variation with doping concentration. In the present investigation, the samples shows ε = 487; tanδ = 1.97 for x = 0.6, and ε = 181; tanδ = 1.01 for x = 0.8, respectively. The observed results can be explained on the basis of composition,relaxationphenomena and super exchange interaction.

Keywords: M-type hexaferrite; co-precipitation method; crystal structure; dielectric properties.

1. Introduction

Current research focuses on altering dielectric, magnetic, and structural properties of hexaferrite by doping different divalent and trivalent cations at iron sites to get suitable saturation magnetization, coercivity, and dielectric properties for specific high-frequency applications. There are several articles on substituting the Fe^{3+} ions by magnetic or non-magnetic 3+ ions but fewer studies on substitution of Fe^{3+} ions by magnetic or non-magnetic 2+ ions in Ba-$SrFe_{12}O_{19}$ hexaferrite. Researchers reported that when trivalent cations such as Ce^{3+} [1], Sm^{3+} [2], Ga^{3+} [3] were substituted for Fe^{3+} ions increased the coercivity of Barium hexaferrite while substituting Al^{3+} [4], and Cr^{3+} [5] at Fe^{3+} decreased the coercivity. The substitution of Fe^{3+} ions by divalent metal cations such as Ca^{2+} [6], Co^{2+} [7], Mn^{2+} [8], Cu^{2+} [9] and Ni^{2+} [10-11] altered the structural, magnetic and dielectric properties. Monitoring of ferrites indicated that their properties are highly affected due to altered chemical composition, distribution of cations in the crystal lattice, and synthesis method.

Different synthesis methods were reported for the preparation of hexaferrite, such as solid-state method [12-15], co-precipitation [16-19], sol-gel [20-22], and microwave hydrothermal [5], each though each method has its advantages and disadvantages. Therefore, in the present investigation, the Fe^{3+} ions were substituted by Ni^{2+} ions in $SrFe_{12}O_{19}$. The

substitution of Fe^{3+} by Ni^{2+} in $SrFe_{12-x}Ni_xO_{19}$ will change the structural, magnetic, and dielectric properties because the ionic size and ionic sates are different for $Fe^{3+}$and Ni^{2+}ions. This substitution may create holes or oxygen vacancies in the system, which leads to a decrease in saturation magnetization. Pratap Behera *et al.* [10] prepared the $BaFe_{12-x}Ni_xO_{19}$(x = 0 - 0.5) hexaferrite by sol-gel method and observed that M_S decreased from 68.16 emu/g (x = 0) to 8.99 emu/g (x = 1) with increase in Ni^{2+}ion concentration. Mousavi Ghahfarokhi *et al.* [11] used the combustion sol-gel method to prepare $SrFe_{12-x}Ni_xO_{19}$ nanoparticles (x = 0 - 1) and found a similar trend in volume and M_S.

The purpose of the present study is to synthesize the uniform distribution of particles using the Co-precipitation method. The Fe^{3+} ions were replaced by Ni^{2+} ions and maintained the stoichiometry of $SrFe_{12-x}Ni_xO_{19}$ ($0.0 \leq x \geq 1.0$) hexaferrite. The impact of Ni^{2+} doping on the dielectric, magnetic, and structural were studied and reported in this paper. Since the ferrites are insulators at room temperature; therefore, their resistivity is high. Ni^{2+} doping into hexaferrite decreases the loss and dielectric constant, making them suitable for microwave devices and as dielectric filler in electromagnetic attenuation materials [23].

2. Materials and Methods

2.1. Experimental method.

In the present work, the $SrNi_xFe_{12-x}O_{19}$ (x = 0.0 – 1.0 @ 0.2 wt%) is synthesized using co-precipitation method. All the precursors used in the synthesis were of analytical grade nitrites. All the salts of ferric nitrate, strontium nitrate, and nickel nitrate were dissolved in deionized water as per the stoichiometry and stirred for 1 hour. A solution of 10 M NaOH was added to the salt solution, and the pH was maintained at ~12, and the stirring was kept sustained. The homogeneity of the mixture was maintained throughout by continuous stirring. The precipitate was filtered and washed several times using deionized water and further with ethanol. Washed precipitates were kept in a hot air oven (Universal itherm A1-7981) at 80 °C overnight. An average yield of 96% was obtained.

Polyvinyl alcohol (binder) of 2 wt.% was mixed with synthesized powders and was pressed uniaxially at 800 kg/cm^2 pressure to form pellets of 1.2 mm thickness and diameter of 8 mm. Sintering of pellets at 1100 °C/4 h was done in a muffle furnace in atmospheric air (Navyug India NIC-4000).

2.2. Structural characterizations.

The X-ray diffraction patterns were recorded for the sintered samples using an X-ray diffractometer (Phillips PAN analytical) with Cu- K_α irradiation (1.5406 Å) in the scanning range of 2θ = 20°-80° with a scan rate of 1°/min at 40 kV and 30 mA. The lattice constants (a&c), X-ray density (d_x), and volume of the unit cell (V) were calculated using the following equations

$$\frac{1}{d^2} = \left\{ \frac{4\left(h^2 + kh + l^2\right)}{3a^2} \right\} + \frac{l^2}{c^2};$$

d_x = 2M/NV; and $V = a^2 c \sin\theta$.

Where h, k, l are miller indices; a&c are lattice constants in Å; d is the interatomic distance in Å; M is the samples molecular weight, N is the Avogadro Number. A technique of non-linear fitting between measured and calculated diffraction patterns based on the crystal structure data

by the least-squares method is known as Rietveld method. Rietveld refinement for all the Ni^{2+} doped hexaferrite samples was carried out using MAUD software [24]. Fourier Transform Infrared (FTIR) spectrum was recorded on Brucker – Tensor 27 spectrometer in the mid-IR range of 4000 – 400 cm^{-1} with a resolution of 4 cm^{-1}. The samples were prepared using KBr pellet method. A 2 mg of sintered powder was mixed with 300 mg of KBr powder (spectroscopic grade) and ground thoroughly to get a homogeneous mixture, which was pressed into 13 mm diameter pellets at 10 tons pressure. The pellets were then heated at 110 °C for 2 to 3 hours. The microstructural analysis was carried out using a Scanning Electron Microscope (SEM) (Tescan, Vega 3 LMU) coupled with energy-dispersive X-ray spectroscopy (EDS) was used for elemental and morphological information. Image J software was used for the in-depth understanding of sample's microstructure (mean grain size, grain size distribution, histograms), and the effect of Ni doping on the granular structure [25]. Measurements of magnetization versus magnetic field (M–H) loops using vibrating sample magnetometer (VSM) Lakeshore 7500, USA at normal temperature was used to study the magnetic properties that include coercive field (H_c), saturation magnetization (M_s), and remnant magnetization (M_r). The frequency variation of dielectric constant and loss (ε & tan δ) were measured using LCR meter (PSM 1705) in the range 10^2– 10^6 Hz at room temperature.

The dielectric constant (ε) was determined using the relation:

$$\varepsilon = Cd/\varepsilon_0 A$$

where C the pellet's capacitance in farads, d is the thickness of the pellet in meters, A the pellets cross-sectional area, and ε_0 the permittivity of free space.

tan $\delta = R_s/\omega L_s$, where ω, R_s and L_s are the angular frequency, circuit resistance and circuit inductance. For good electrical contacts for measurements, the sintered pellets were coated with silver paste with approximately 1 µm thickness.

3. Results and Discussion

3.1. XRD analysis.

XRD is a versatile and non-destructive technique used for phase identification, measurement of crystallite size, and other structural parameters. Fig. 1 (a) displays the XRD patterns of Ni^{2+} doped $SrFe_{12}O_{19}$ (x = 0 to 1 with intervals 0.20) in which all diffraction peaks were indexed with JCPDS card No's: 33-1340 within space group $P6_3/mmc$ (no.194) ($SrFe_{12}O_{19}$), 33- 0664 (α-Fe_2O_3) and 73-1523 (NiO), 74-1913 ($NiFe_2O_4$), and it is found that all the peaks were matched well with the hexaferrite phase.

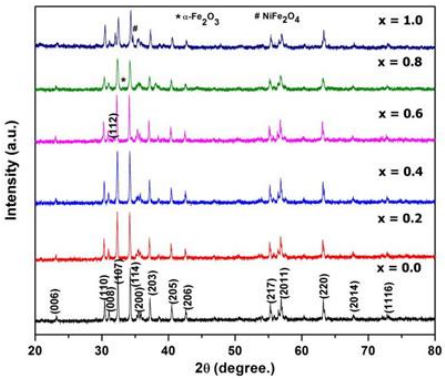

Figure 1. (a) X-ray diffraction patterns of Ni^{2+}substituted $SrFe_{12}O_{19}$ ($0.0 \leq x \geq 1.0$) hexaferrites.

The miller indices (1 0 7) and (1 1 4) are the characteristic peaks of $SrFe_{12}O_{19}$. No impurity phases were observed for x = 0.0 up to 0.4 concentration. At higher concentrations ($x \geq 0.6$) of Ni^{2+} ions doping, the secondary phases such as α-Fe_2O_3 and $NiFe_2O_3$ were observed. The $NiFe_2O_3$ phase is dominant at higher (x = 1.0) dopant concentrations [11] due to smaller strontium hexaferrite units similar to S-shaped cubic block having spinel-like structure and R shaped hexagonal block containing Sr ions. The additional α-Fe_2O_3 phase (2θ = 33.10°) is observed, and it is more prominent at higher concentrations of Ni^{2+} doping. The charge neutrality in hexaferrite occurs when one cation replaces another cation compensating Fe ions ($Fe^{2+} \leftrightarrow Fe^{3+}$) [26] among them. When Fe^{3}+ ions are replaced by Ni^{2+} ions at B sites probability of Fe^{2+} reacting with oxygen to form a-Fe_2O_3 phase is high, which is evident from XRD (Fig.1a). There is no effect of the hematite phase on the magnetic properties of current samples since it is non-magnetic.

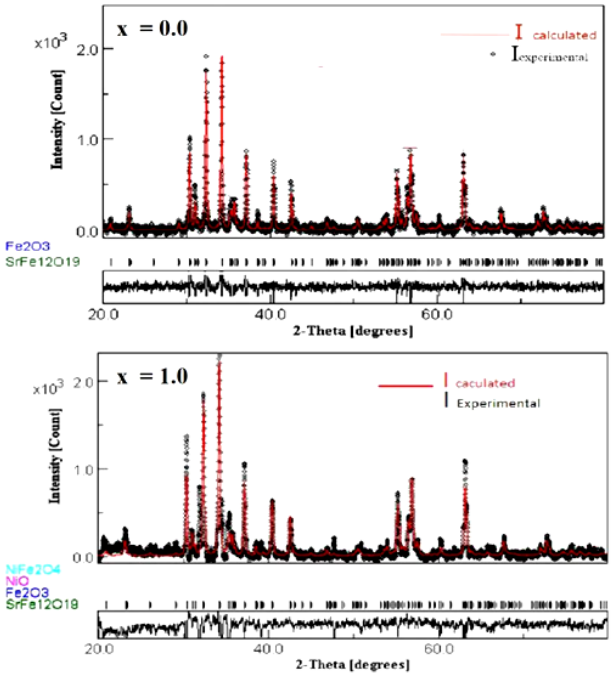

Figure 1. (b) Rietveld refinement of Ni^{2+}substituted $SrFe_{12}O_{19}$ (x = 0.0 & 1.0) hexaferrites.

Figure 1(b) shows the Rietveld refinements for sample x = 0.0 and 1.0. Rietveld refinements of XRD patterns for all samples were carried out using MAUD software using $P6_3/mmc$ space group and R3c used for the second phase, which indicated a good correlation between calculated and experimental data. The lattice parameter (a&c), R_p (profile fitting R-value), R_{wp}(Weighted profile R-Value), R_{Bragg} (Bragg value), R_{exp} (expected value),Sig (goodness of fit (GOF) quality factor), X-ray density (d_x), and unit cell volume (V) were tabulated in Table 1. The least values of R_p, R_{wp},and Sig(GOF) indicate good quality samples and effective refinement. The increase in lattice constants with the addition of Ni^{+2} (0.69 Å) is because of Ni^{+2} ionic radius being greater than that of Fe^{+3} (0.645 Å) ions [10]. Our results are comparable with Pratap Behera *et al.* [10], where they reported an increase in the lattice parameters with Ni^{+2} doping in Barium hexaferrite synthesized using sol-gel method and sintered at 1150 ºC / 12 h. Mousavi Ghahfarokhi *et al.* [11] prepared $SrFe_{12-x}Ni_xO_{19}$ nanoparticles (x = 0.0 - 1.0) by a combustion Sol-gel method. The changes in unit cell volume (V) with Ni^{+2} doping is due to the incorporation of Ni^{2+} ions into the unit cell of $SrFe_{12}O_{19}$ confirms that $Fe^{2+/3+}$ ions are replaced by Ni^{2+} ions. The c/a ratio is less than 3.98, which shows

that the present samples belong to a hexagonal structure [27]. The changes in X-ray density with Ni^{2+} doping are due to the changes in the molar mass of the sample [28].

Table 1. The lattice parameters *a* and *c*, unit cell volume (*V*), X-ray density (d_x), and Rietveld refinement parameters of $SrFe_{12-x}Ni_xO_{19}$ samples.

Parameters	***x* = 0.0**	***x* = 0.2**	***x* = 0.4**	***x* = 0.6**	***x* = 0.8**	***x* = 1.0**
R_p(%)	1.38	1.65	2.45	2.22	2.02	2.21
R_{wp}(%)	1.54	1.45	3.05	1.68	2.52	2.73
R_{Brag}(%)	1.35	1.34	1.86	1.55	2.03	2.45
R_{exp}(%)	10.22	11.20	10.54	10.74	11.51	11.56
Sig (GOF)	1.38	1.37	2.90	1.54	2.19	2.35
a (Å)	5.879	5.881	5.880	5.884	5.886	5.883
c (Å)	23.0468	23.0478	23.0620	23.0627	23.0695	23.0510
c/a	3.920	3.919	3.922	3.919	3.919	3.918
V (Å^3)	689.82	690.32	690.51	691.47	692.14	690.88
d_x (g/cm^3)	5.100	5.109	5.116	5.107	5.094	5.103
Avg grain size (μm) from SEM	1.713	1.470	0.902	0.776	1.274	0.549

3.2. SEM and EDS analysis.

Fig.2 shows the SEM micrographs, histograms of grain size of $SrNi_xFe_{12-x}O_{19}$ (*x* = 0.0 -1.0), and energy dispersive spectrum (EDS).

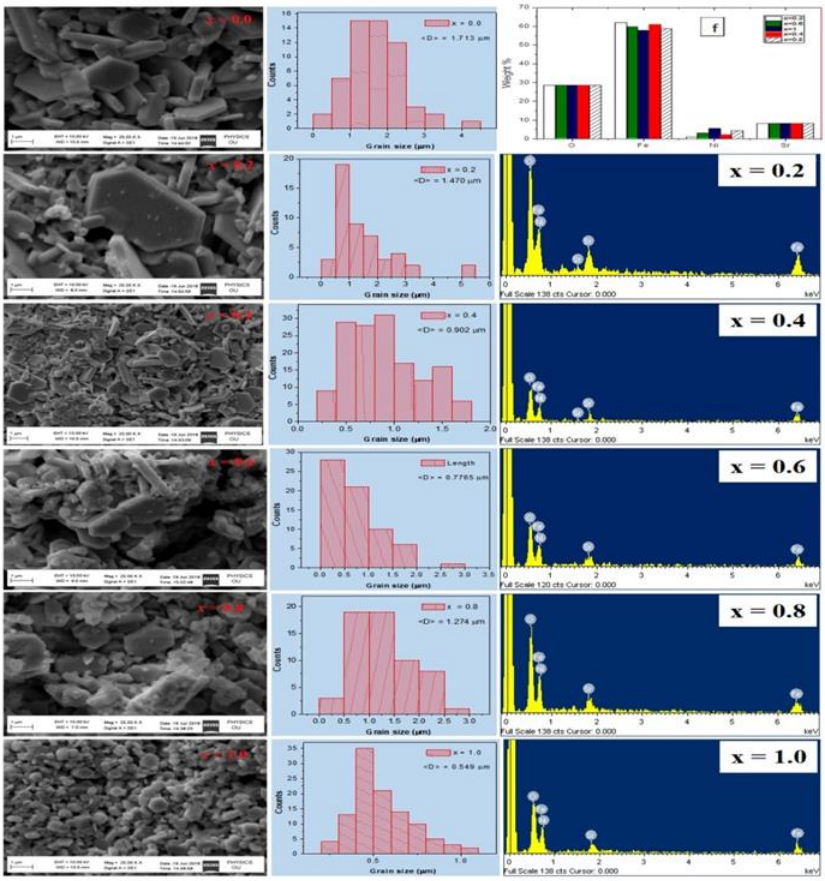

Figure 2. SEM images (0.0 ≤ x ≤ 1), histogram of grain size (0.0 ≤ x ≤ 1) and EDS of Ni^{2+} doped $SrFe_{12}O_{19}$ (0.2 ≤ x ≤ 1) hexaferrites.(f) represents the histogram for wt% percentage of the elements with varying composition.

It clearly shows that the grains have a hexagonal shape (plate-like structure for *x*). The values of average grain sizes are listed in Table 1 and found between 1.713 (*x* = 0) – 0.49 μm (*x* = 1.0). The hexagonal shape is clearly seen for *x* = 0.0 to 0.6 and *x* > 0.2, the particles are agglomerated. Along with a hexagonal plate-like structure, a small amount of α-Fe_2O_3 and

$NiFe_2O_4$ (seen in XRD, Fig. 1a) can be seen. With Ni^{2+} doping, the agglomeration of grains increased. The variation in grain size was due to the agglomeration of the particle collections, which resulted in inhomogeneous size distribution.

Energy Dispersive X-ray Spectroscopy (EDS) is a technique of analyzing an element that can give information related to the chemical composition of a sample. It is a qualitative as well as a quantitative technique. Confirmation of chemical composition of $SrNi_xFe_{12-x}O_{19}$ (x = 0.2 - 1.0 in steps of 0.2 wt%) can be done through the quantitative elemental analysis by using EDS spectrometer attached to the SEM for all samples. Table 2 shows the estimated and obtained EDS results for doped samples indicating atomic percentage (wt %) of Ni, Sr, O, and Fe, which correlate with designed composition, and these elements are found to be evenly distributed throughout the entire area, which reveals uniform chemical phase.

Table 2. EDS data for Ni substituted $SrFe_{12}O_{19}$hexaferrites.

Sample	Estimated wt % of elements				Obtained wt % of elements from EDS			
	Sr	Fe	Ni	O	Sr	Fe	Ni	O
x = 0.2	8.248	62.032	1.105	28.615	8.248	61.890	1.100	28.760
x = 0.4	8.243	60.948	2.209	28.599	8.243	60.775	2.205	28.59
x = 0.6	8.239	59.867	3.310	28.584	8.239	59.980	3.298	28.49
x = 0.8	8.235	58.784	4.413	28.568	8.235	58.792	4.360	28.46
x = 1.0	8.230	57.703	5.513	28.554	8.230	57.810	5.454	28.5

3.3. FTIR analysis.

Figure 3, depicts FTIR spectra for Ni^{2+} doped $SrFe_{12}O_{19}$ ($0.0 \leq x \leq 0.8$) measured in the range 400–4000 cm^{-1}. The absorption bands are seen between 590 cm^{-1}–610 cm^{-1} and 400cm^{-1}–450 cm^{-1} were due to tetrahedral and octahedral bands of hexaferrite.

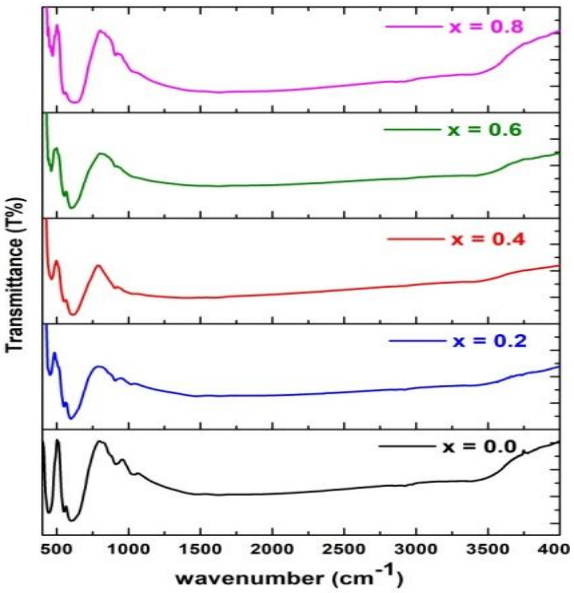

Figure 3 FTIR spectrum for Ni^{2+} doped $SrFe_{12}O_{19}$ ($0.0 \leq x \leq 0.8$) hexaferrites.

The changes in the tetrahedral and octahedral bands are due to the changes that occurred in the Fe^{3+} - O^{2-} bands because of Ni^{2+} doping [29]. The bands of metal-oxygen stretching vibrations are observed around 550 cm^{-1} and 590 cm^{-1} show the formation of hexagonal structure [30]. The peak shift to the higher wavenumber side is due to the distance between Fe^{3+} and O^{2-} ions with increasing doping concentration. The stretching and bending vibration band of Sr-O and Fe-O observed around 910 cm^{-1} and 1020 cm^{-1}, respectively [31]. The band intensity decreased with Ni^{2+} doping concentration are due to ionic replacement and changes

in the magnetic dipole moment. Fig. 3 also shows two bands at 1388 cm^{-1} and at 3400 cm^{-1} corresponds to NO^{3-} stretching vibration and O-H group, respectively.

3.4. Magnetic studies.

Fig. 4(a) shows the hysteresis loops of Ni^{2+} doped $SrFe_{12}O_{19}$ ($0.0 \leq x \geq 0.8$) at room temperature, indicating that the samples are magnetically ordered. The saturation magnetization (M_S), remanence (M_r), the ratio of M_r/M_S, and coercivity (H_C) were tabulated in Table 3. It is clear from Fig. 4(b) that saturation and remnant magnetization decreased with x up to 0.6 and then increased with further doping of Ni^{2+}. The value of M_S decreases from 68 to 50 emu/g ($x = 0.0$ to $x = 0.6$) and for $x > 0.6$, M_S is increased to 64 emu/g ($x = 0.8$). In hexaferrite, one tetrahedral ($4f_1$), three octahedral (2a, 12k, and $4f_2$), and one trigonalbipyramidal (2b) sites are present. Three sites (2a, 12k and 2b) are of parallel (spin up, ↑) while two sites ($4f_1$ and $4f_2$) are of antiparallel spins (spin down, ↓) [9]. The ferromagnetic structure is formed by a superexchange interaction between the iron atoms in the structural sites through O^{2-} ions [32]. The increase of Ni^{2+}cations replaces Fe^{3+} ions, ($x = 0$ to 0.6), the saturation magnetization (M_S) decreased as the magnetic moment per unit volume decreased. For $x > 0.6$, M_S is increased because, at higher concentrations of x, a very small amount of $NiFe_2O_3$ as a secondary phase is formed (seen in XRD, Fig.1). The substitution of higher concentration of Ni^{2+} ions increase the superexchange interaction between Fe^{3+} ions at spin up sites and therefore the M_S increased from 50 emu/g ($x = 0.6$) to 64 emu/g ($x = 0.8$).

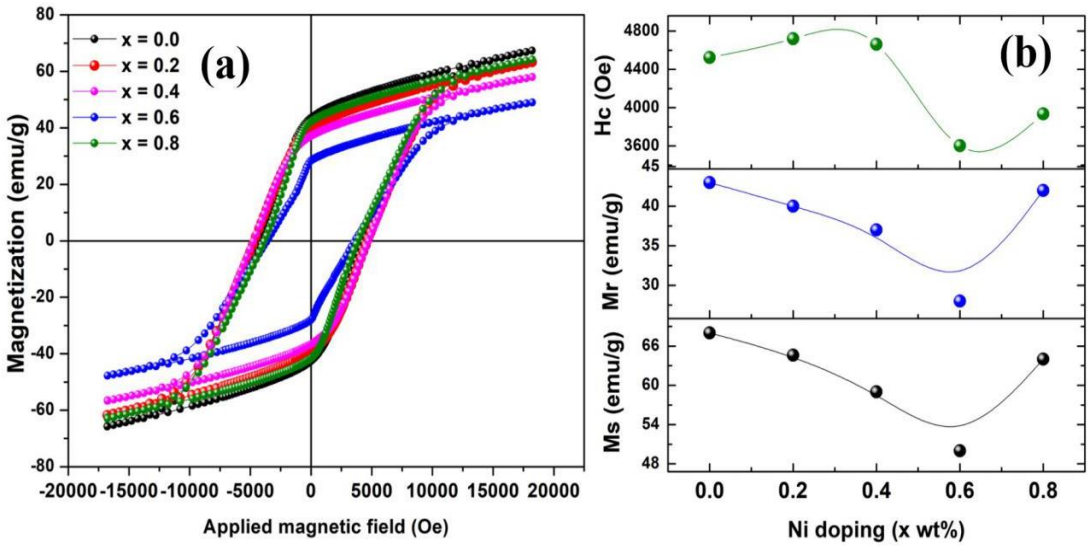

Figure 4. (a) Room temperature magnetic hysteresis loops of $SrNi_xFe_{12-x}O_{19}$ ($0.0 \leq x \geq 0.8$) (b) Dependence of Magnetic data (M_s, M_r, and H_c) with Ni^{2+}substitution.

The range of squareness ratio (M_r/M_S) between 0.560-0.656 confirms the single domain of prepared samples [33-36]. The coercivity (H_C) increased anisotropically with doping. The value of H_C increased for $x = 0.2$ and then decreased upto$x = 0.6$ and for $x = 0.8$, H_C increased again. The substitution of ions at octahedral (12k, 4f2) and trigonal bi-pyramidal (2b) sites contributes to magnetocrystalline anisotropy in hexaferrite. The decrease in coercivity for x = 0.2 to 0.6 may be related to the magnetocrystalline anisotropy field [9]. The increase in H_C for $x = 0.8$ is due to the formation of impurity phases, which is evident from XRD (Fig.1a) and SEM (Fig. 2), respectively.

Table 3. Room temperature data of M_s, M_r, H_c, ε and tanδ (at 100 Hz) for Ni^{2+} doped strontium hexaferrite.

x	M_s (emu/g)	M_r (emu/g)	M_r/M_s	H_c (Oe)	ε	tanδ
0.0	68	43	0.632	4525	14531	6.13
0.2	65	40	0.615	4720	10338	4.77
0.4	59	37	0.627	4662	4489	4.50
0.6	50	28	0.560	3602	487	1.97
0.8	64	42	0.656	3936	181	1.01

3.5. Dielectric studies.

Fig. 5(a & b) shows the frequency variation of dielectric constant (ε) and tanδ for $SrNi_xFe_{12-x}O_{19}$ (x = 0.0 - 0.8) at room temperature measured between 10^2 to 10^6 Hz.

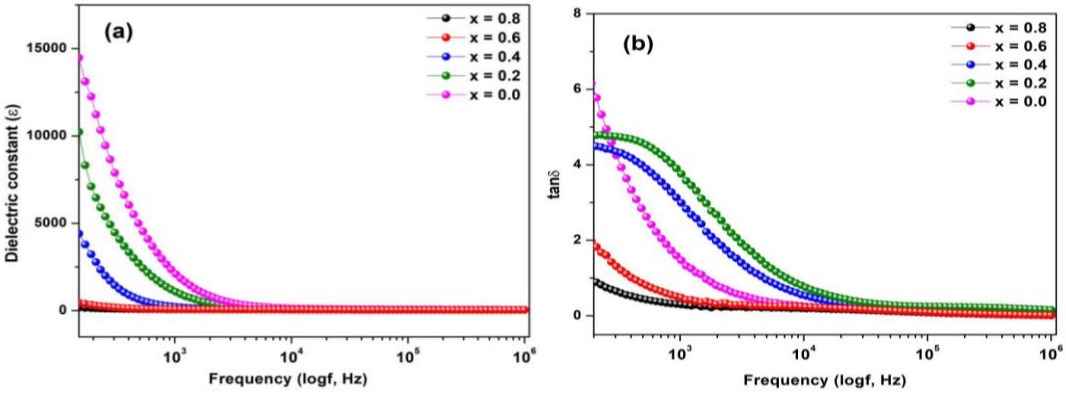

Figure 5. (a) Dielectric constant (ε') and (b) tanδ as a function of log *f* (Hz) for $SrNi_xFe_{12-x}O_{19}$ hexaferrite at room temperature.

Figure 5a indicates a high value of ε at 100 Hz and a low value above 1kHz due to the relaxation process accompanied by a relaxation peak observed in Fig. 5b (x = 0.4 & 0.6). Space charge polarization decreases ε value with frequency increase. The decrease in ε at a higher frequency is due to the lag in the change in orientation of the dipoles due to the inertial and spatially oriented defects [37]. The values of dielectric constant (ε) and tanδ at 100 Hz are given in Table 3. It is observed that ε and tanδ decreased with Ni^{2+} doping. Iwauchi [38] reported that in ferrites, the conduction mechanism and polarization are similar. It is reported that the hopping of electrons between Fe^{2+}/Fe^{3+} at octahedral sites takes place in the conduction mechanism, whereas dielectric polarization might be due to conduction between positive holes and electrons that arise due to oxygen loss during sintering and/or substitution of metal ions [28]. The doping of Ni^{2+} ions into hexaferrite decreased dielectric constant and loss. In the present investigation, the samples shows ε = 487; tanδ = 1.97 for x = 0.6, and ε = 181; tanδ = 1.01 for x = 0.8, respectively. The penetration depth of electromagnetic waves can be decreased by the materials possess a high dielectric constant. Therefore, the materials with lower dielectric constant and loss can be useful at high frequency [39-41].

4. Conclusions

The $SrNi_xFe_{12-x}O_{19}$ ($0.0 \leq x \geq 1.0$) hexaferrites were synthesized using Co-precipitation method and densified at 1100 ºC/4h using conventional sintering method. No impurity phases were observed for x = 0.0 upto 0.4 concentration but for $x \geq 0.6$, secondary phases were observed. The changes in lattice parameters were due to the difference in the ionic radii. The values of average grain sizes are found between 1.713 (x = 0) – 0.49 µm (x = 1.0). The M_S decreased with x upto 0.6 and for x> 0.6, M_S increased. The decrease in coercivity for x = 0.2

to 0.6 is may be related to the magnetocrystalline anisotropy field. The squareness ratio (M_r/M_S) range between 0.560 - 0.656 confirming single domain of prepared samples. It is observed that ε and tanδ decreased with Ni^{2+} doping. In the present investigation, the samples shows ε = 487; tanδ = 1.97 for x = 0.6, and ε = 181; tanδ = 1.01 for x = 0.8, respectively.

Funding

This research received no external funding.

Acknowledgments

Maramu Nyathani conveys his sincere thanks to Prof. D. Ravinder & Sadhana K for their enthusiastic encouragement and guidance to pursue Ph.d. The authors are also grateful to the Head Department of Physics, University College of Science, Osmania University, Hyderabad.

Conflicts of Interest

The authors declare no conflict of interest.

References

1. Pawar, R.A.; Desai, S.S.; Tamboli, Q.Y.; Shirsath, S.E.; Patange, S.M. Ce3+ incorporated structural and magnetic properties of M type barium hexaferrites. *Journal of Magnetism and Magnetic Materials* **2015**, *378*, 59-63, https://doi.org/10.1016/j.jmmm.2014.10.166.
2. Wang, L.; Zhang, J.; Zhang, Q.; Xu, N.; Song, J. XAFS and XPS studies on site occupation of Sm3+ ions in Sm doped M-type BaFe12O19. *Journal of Magnetism and Magnetic Materials* **2015**, *377*, 362-367, https://doi.org/10.1016/j.jmmm.2014.10.097.
3. Bsoul, I.; Mahmood, S.H. Magnetic and structural properties of BaFe12−xGaxO19 nanoparticles. *Journal of Alloys and Compounds* **2010**, *489*, 110-114, https://doi.org/10.1016/j.jallcom.2009.09.024.
4. Dhage, V.N.; Mane, M.L.; Keche, A.P.; Birajdar, C.T.; Jadhav, K.M. Structural and magnetic behaviour of aluminium doped barium hexaferrite nanoparticles synthesized by solution combustion technique. *Physica B: Condensed Matter* **2011**, *406*, 789-793, https://doi.org/10.1016/j.physb.2010.11.094.
5. Katlakunta, S.; Meena, S.S.; Srinath, S.; Bououdina, M.; Sandhya, R.; Praveena, K. Improved magnetic properties of Cr3+ doped SrFe12O19 synthesized via microwave hydrothermal route. *Materials Research Bulletin* **2015**, *63*, 58-66, https://doi.org/10.1016/j.materresbull.2014.11.043.
6. Moon, K.-S.; Lim, E.-S.; Kang, Y.-M. Effect of Ca and La substitution on the structure and magnetic properties of M-type Sr-hexaferrites. *Journal of Alloys and Compounds* **2019**, *771*, 350-355, https://doi.org/10.1016/j.jallcom.2018.08.306.
7. Chavan, V.C.; Shirsath, S.E.; Mane, M.L.; Kadam, R.H.; More, S.S. Transformation of hexagonal to mixed spinel crystal structure and magnetic properties of Co2+ substituted BaFe12O19. *Journal of Magnetism and Magnetic Materials* **2016**, *398*, 32-37, https://doi.org/10.1016/j.jmmm.2015.09.002.
8. Sharma, P.; Rocha, R.A.; Medeiros, S.N.; Hallouche, B.; Paesano, A. Structural and magnetic studies on mechanosynthesized BaFe12−xMnxO19. *Journal of Magnetism and Magnetic Materials* **2007**, *316*, 29-33, https://doi.org/10.1016/j.jmmm.2007.03.207.
9. Rafiq, M.A.; Waqar, M.; Muhammad, Q.K.; Waleed, M.; Saleem, M.; Anwar, M.S. Conduction mechanism and magnetic behavior of Cu doped barium hexaferrite ceramics. *Journal of Materials Science: Materials in Electronics* **2018**, *29*, 5134-5142, https://doi.org/10.1007/s10854-017-8477-y.
10. Behera, P.; Ravi, S. Effect of Ni doping on structural, magnetic and dielectric properties of M-type barium hexaferrite. *Solid State Sciences* **2019**, *89*, 139-149, https://doi.org/10.1016/j.solidstatesciences.2019.01.003.
11. Mousavi Ghahfarokhi, S.E.; Hosseini, S.; Zargar Shoushtari, M. Fabrication of SrFe12−xNixO19 nanoparticles and investigation on their structural, magnetic and dielectric properties. *International Journal of Minerals, Metallurgy, and Materials* **2015**, *22*, 876-883, https://doi.org/10.1007/s12613-015-1145-4.
12. Singh, J.; Singh, C.; Kaur, D.; Zaki, H.; Abdel-Latif, I.A.; Narang, S.B.; Jotania, R.; Mishra, S.R.; Joshi, R.; Dhruv, P.; Ghimire, M.; Shirsath, S.E.; Meena, S.S. Elucidation of phase evolution, microstructural, Mössbauer and magnetic properties of Co2+Al3+ doped M-type BaSr hexaferrites synthesized by a ceramic method. *Journal of Alloys and Compounds* **2017**, *695*, 1112-1121, http://dx.doi.org/10.1016/j.jallcom.2016.10.237.

13. Huang, K.; Yu, J.; Zhang, L.; Xu, J.; Li, P.; Yang, Z.; Liu, C.; Wang, W.; Kan, X. Synthesis and characterizations of magnesium and titanium doped M-type barium calcium hexaferrites by a solid state reaction method. *Journal of Alloys and Compounds* **2020**, *825*, 154072, https://doi.org/10.1016/j.jallcom.2020.154072
14. Karahroudi, Z.H.; Kambiz, H.; Goodarzi, M. Green synthesis and characterization of hexaferrite strontium-perovskite strontium photocatalyst nanocomposites. *Main Group Metal Chemistry*, **202**0, *43*, 26-42, https://doi.org/10.1515/mgmc-2020-0004.
15. Luthfianti, H.R.; Widanarto, W.; Ghoshal, S.K.; Effendi, M.; Cahyanto, W.T.; Magnetic and microwave absorption properties of Mn4+ doped barium-natural ferrites prepared by the modified solid-state reaction method, *Journal of Physics: Conference Series*, **2020**, *1494*, 012043, https://doi.org/10.1088/1742-6596/1494/1/012043
16. Ajeesha, T.L.; Anantharaman, A.; Baby, J.N.; George, M. Structural, Magnetic, Electrical and Photo-Fenton Properties of Copper Substituted Strontium M-Hexagonal Ferrite Nanomaterials via Chemical Coprecipitation Approach. *Journal of Nanoscience and Nanotechnology* **2020**, *20*, 1589-1604, https://doi.org/10.1166/jnn.2020.17132.
17. Susilawati, Doyan, A.; Taufik, M.; Wahyudi. The structure of barium M-hexaferrite ($BaFe_{12-2x}Co_xNi_xO_{19}$) powders using co-precipitation methods, *AIP conference proceedings*, **2020**, *2251*, 040028, https://doi.org/10.1063/5.0015750
18. Tran, N.; Lee, M.Y.; Lee, B.W. Microwave absorption properties of cobalt-doped $BaFe_{12}O_{19}$ hexaferrites. *Journal of Korean Physical Society*, **2020**, *77*, 1125–1134, https://doi.org/10.3938/jkps.77.1125
19. Sagayaraj, R.; Dhineshkumar, T.; Prakash, A.; Aravazhi, S.; Chandrasekaran, G.; Jayarajan, D.; Sebastian, S.; Fabrication, microstructure, morphological and magnetic properties of W-type ferrite by co-precipitation method: Antibacterial activity, *Chemical Physics Letters*, **2020**, *759*, 137944. https://doi.org/10.1016/j.cplett.2020.137944
20. Wong, Y.C.; Wang, J.; Teh, G.B. Structural and Magnetic Studies of SrFe12O19 by Sol-gel Method. *Procedia Engineering* **2014**, *76*, 45-52, https://doi.org/10.1016/j.proeng.2013.09.246.
21. Al-Hwaitat E.S.; Dmour, M.K.; Bsoul, I.; Al-Buqain, R.; Mahmood, S.H.; A comparative study of BaxSr1−xFe12O19 ferrite permanent magnets prepared by ball milling and sol–gel routes, *Journal of Physics D: Applied Physics*, **2020**, *53*, 364001, https://doi.org/10.1088/1361-6463/ab9135
22. Bankar, S.B.; Meshram, N.S.; Nandanwar, A.K.; Ahamad, H.S.; Dhoble S.J.; Rewatkar K.G. Synthesis and Characterization of Nanocrystalline $Ca_2Cu_2Fe_{(12-x)}Al_xO_{22}$ Y-Type Hexaferrites by the Sol–Gel Combustion Method, *Integrated Ferroelectrics*, **2020**, *212*, 25-30, https://doi.org/10.1080/10584587.2019.1674985
23. Iqbal, M.J.; Farooq, S. Enhancement of electrical resistivity of Sr0.5Ba0.5Fe12O19 nanomaterials by doping with lanthanum and nickel. *Materials Chemistry and Physics* **2009**, *118*, 308-313, https://doi.org/10.1016/j.matchemphys.2009.07.056.
24. Lutteroti, L. MAUD tutorial-Instrumental broadening determination, **2006**, 1-18 http://www.ing.unitn.it/~maud
25. Schneider, C.A.; Rasband, W.S.; Eliceiri, K.W. NIH Image to ImageJ: 25 years of image analysis. *Nat Methods* **2012**, *9*, 671-675, https://doi.org/10.1038/nmeth.2089.
26. Chawla, S.K.; Meena, S.S.; Kaur, P.; Mudsainiyan, R.K.; Yusuf, S.M. Effect of site preferences on structural and magnetic switching properties of CO–Zr doped strontium hexaferrite SrCoxZrxFe(12−2x)O19. *Journal of Magnetism and Magnetic Materials* **2015**, *378*, 84-91, http://dx.doi.org/10.1016/j.jmmm.2014.10.168.
27. Teh, G.B.; Wong, Y.C.; Tilley, R.D. Effect of annealing temperature on the structural, photoluminescence and magnetic properties of sol–gel derived Magnetoplumbite-type (M-type) hexagonal strontium ferrite. *Journal of Magnetism and Magnetic Materials* **2011**, *323*, 2318-2322, https://doi.org/10.1016/j.jmmm.2011.04.014.
28. Ashiq, M.N.; Iqbal, M.J.; Gul, I.H. Structural, magnetic and dielectric properties of Zr–Cd substituted strontium hexaferrite (SrFe12O19) nanoparticles. *Journal of Alloys and Compounds* **2009**, *487*, 341-345, https://doi.org/10.1016/j.jallcom.2009.07.140.
29. Josyulu, O.S.; Sobhanadri, J. The far-infrared spectra of some mixed cobalt zinc and magnesium zinc ferrites. *physica status solidi (a)* **1981**, *65*, 479-483, https://doi.org/10.1002/pssa.2210650209.
30. Baykal, A.; Güngüneş, H.; Sözeri, H.; Amir, M.; Auwal, I.; Asiri, S.; Shirsath, S.E.; Demir Korkmaz, A. Magnetic properties and Mössbauer spectroscopy of Cu-Mn substituted BaFe12O19 hexaferrites. *Ceramics International* **2017**, *43*, 15486-15492, https://doi.org/10.1016/j.ceramint.2017.08.096.
31. Waldron, R.D. Infrared Spectra of Ferrites. *Physical Review* **1955**, *99*, 1727-1735, https://doi.org/10.1103/PhysRev.99.1727.
32. Lechevallier, L.; Le Breton, J.M.; Wang, J.F.; Harris, I.R. Structural analysis of hydrothermally synthesized Sr1−xSmxFe12O19 hexagonal ferrites. *Journal of Magnetism and Magnetic Materials* **2004**, *269*, 192-196, https://doi.org/10.1016/S0304-8853(03)00591-2.

33. Kagdi, A.R.; Solanki, N.P.; Carvalho, F.E.; Meena, S.S.; Bhatt, P.; Pullar, R.C.; Jotania, R.B. Influence of Mg substitution on structural, magnetic and dielectric properties of X-type bariumzinc hexaferrites Ba2Zn2-xMgxFe28O46. *Journal of Alloys and Compounds* **2018**, *741*, 377-391, https://doi.org/10.1016/j.jallcom.2018.01.092.
34. Gaffoor, A.; Naidu, K.C.B.; Ravinder, D.; Batoo, K.M.; Adil, S.F.; Khan, M. Synthesis of nano-NiXFe2O4 (X = Mg/Co) by citrate-gel method: structural, morphological and low-temperature magnetic properties. *Applied Physics A* **2019**, *126*, https://doi.org/10.1007/s00339-019-3225-1.
35. Boda, N.; Naidu, K.C.B.; Basha, D.B.; Ravinder, D. Structural and Magnetic Properties of CdCoFe2O4 Nanoparticles. *Journal of Superconductivity and Novel Magnetism* **2020**, *33*, 1039-1044, https://doi.org/10.1007/s10948-019-05242-1.
36. Kumar, D.R.; Lincoln, C.A.; Ravinder, D.; Ahmad, S.I. Structural, morphological, luminescence, magnetic, and electrical transport properties of zinc-doped MnFe2O4 nanomaterials. *Applied Physics A* **2020**, *126*, https://doi.org/10.1007/s00339-020-03894-8.
37. Cernea, M.; Florentina Negrea, R.; Veronica Ciuchi, I.; Baldisserri, C.; Trusca, R.; Galassi, C. Dielectric characterization of BaxSr1−xFe12O19 (x=0.05−0.35) ceramics. *Ceramics International* **2016**, *42*, 1050-1056, https://doi.org/10.1016/j.ceramint.2015.09.029.
38. Iwauchi, K. Dielectric Properties of Fine Particles of Fe3O4and Some Ferrites. *Japanese Journal of Applied Physics* **1971**, *10*, 1520-1528, https://doi.org/10.1143/JJAP.10.1520**.**
39. Iqbal, M.J.; Ashiq, M.N. Physical and electrical properties of Zr–Cu substituted strontium hexaferrite nanoparticles synthesized by co-precipitation method. *Chemical Engineering Journal* **2008**, *136*, 383-389, https://doi.org/10.1016/j.cej.2007.05.046.
40. Ansari, M.M.N.; Khan, S.; Ahmad, N. Structural, electrical transport and magnetic properties of Nd3+ substituted Mn–Cu nanoferrites. *Journal of Alloys and Compounds* **2020**, *831*, https://doi.org/10.1016/j.jallcom.2020.154778.
41. Noor, A.; Akhtar, M.N.; Khan, S.N.; Nazir, M.S.; Yousaf, M. Synthesis, morphological and electromagnetic evaluations of Ca doped Mn spinel nanoferrites for GHz regime applications. *Ceramics International* **2020**, *46*, 13961-13968, https://doi.org/10.1016/j.ceramint.2020.02.194.